An organisational principle for cortical receptive fields

Daniel Gramm Kristensen[1] and Kristian Sandberg[1,2]

[1] Center of Functionally Integrative Neuroscience, Department of Clinical Medicine, Aarhus University, Aarhus, Denmark.

[2] Hammel Neurorehabilitation and Research Centre, Aarhus University Hospital, Hammel, Denmark.

Corresponding author

Daniel Gramm Kristensen

Center of Functionally Integrative Neuroscience

Aarhus University Hospital

Nørrebrogade 44, Building 10G

8000 Aarhus C

Denmark

Email: dgramm@cfin.au.dk

Acknowledgements

The authors would like to thank Dr. Sam Schwarzkopf and Dr. Martin Dietz for assistance with data collection and analysis.

Conflict of interest

The authors declare no conflicts of interest.

Visual receptive fields are characterised by their centre-surround organisation and are typically modelled by Difference-of-Gaussians (DoGs)[1]. The DoG captures the effect of surround modulation, where the central receptive field can be modulated by simultaneous stimulation of a surrounding area[2–5]. Although it is well-established that this centre-surround organisation is crucial for extracting spatial information from visual scenes, the underlying law binding the organisation has remained hidden. Indeed, previous studies have reported a wide range of size and gain ratios of the DoG used to model the receptive fields[6–9]. Here, we present an equation that describes a principle for receptive field organisation, and we demonstrate that functional Magnetic Resonance Imaging (fMRI) population Receptive Field (pRF) maps of human V1 adhere to this principle. We formulate and understand the equation through consideration of the concept of Direct-Current-free (DC-free) filtering from electrical engineering, and we show how this particular type of filtering effectively makes the DoG process frequencies of interest without misallocation of bandwidth to redundant frequencies. Taken together, our results reveal how this organisational principle enables the visual system to adapt its sampling strategy to optimally cover the stimulus-space relevant to the organism, restricted only by Heisenberg's uncertainty principle that imposes a lower bound on the simultaneous precision in spatial position and frequency. Since surround modulation has been observed in all sensory modalities[10], we expect these results will become a corner stone in our understanding of how biological systems in general achieve their high information processing capacity.

Surround modulation, an elementary computation of the visual system, is believed to be key to our understanding of how biological systems process information, but its precise role is unclear. Surround modulation can be modelled with a Difference of Gaussians (DoG) that consists of a small central, positive Gaussian surrounded by a larger, negative Gaussian. The size ratio of these two Gaussians is parameterised by the standard deviations of the negative, larger Gaussian (σ_2) divided by the positive, smaller Gaussian (σ_1). In our use of the model, the gain ratio is parameterised by a multiplier, δ, that modulates the amplitude of the negative larger Gaussian (see Methods for specifics on the model employed here).

In the frequency domain, a DoG can be viewed as a bandpass filter[11]. To characterize this filter, three primary parameters of interest must be considered: the peak frequency of the filter, its bandwidth at full-width at half-maximum (FWHM), and its amplitude. The peak frequency defines the spatial frequency to which the pRF is most responsive. The bandwidth is a measure of how broad a range of frequencies the pRF responds to, and in the present context the amplitude can be understood as how sensitive the filter is to the peak frequency.

When dealing with filters, it is of particular interest how the filters treat constant signals, i.e. the Direct-Current component. The DC-component in the spatial domain corresponds to signals of constant intensity over distance and is in most instances the signal average. In the frequency domain, the constant signals are contained in frequencies of zero cycles per unit distance. The signal DC-component is often considered redundant information, and thus might claim processing resources unnecessarily – something we will explore in greater detail later. There are three main ways to characterise the behaviour of the DC component. These characteristics can be illustrated with sinusoidal signals (we will later apply these concepts to filters) as in Figure 1A for the spatial domain. First, in green, is the DC-biased signal where the DC component increases as a function of distance (this, of course, depends on the interval used for the analysis, but here a moving average of one period is considered). Next, in blue, is the DC-offset signal, where the DC-component is constant, but non-zero. Last, in black, is the DC-free signal that has no DC-component, or, more accurately, has an average value of zero due to its oscillations of equal positive and negative amplitude centred on zero. In some areas of the literature, DC-bias and DC-offset is used interchangeably[12], but here we introduce a

distinction between the two concepts in order to specify more precisely what signifies DC-free filtering. Figure 1B illustrates how these three signals behave in the frequency domain. The DC-biased signal shows a peak at 10 cycles, but also a large peak at 0 cycles that slowly tapers off. The DC-offset signal has two features; a peak at 0 cycles and at 2.5 cycles. Finally, and most importantly, the DC-free signal only shows a peak at 5 cycles, i.e. there are no components at 0 cycles.

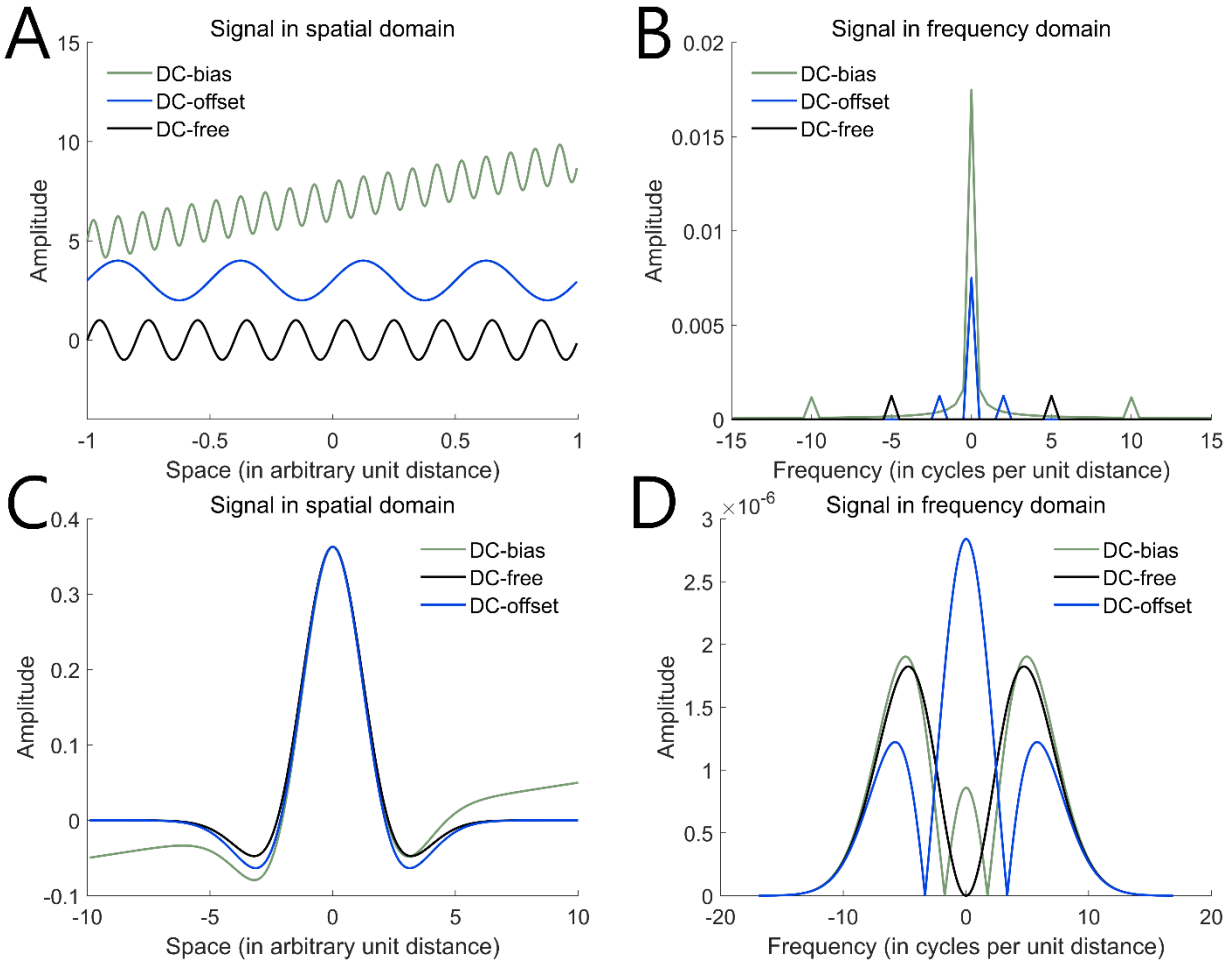

Figure 1. DC-component characteristics. A: DC-biased, DC-offset and DC-free sinusoidal signals in the spatial domain. **B:** Same as A, but in the frequency domain. **C:** DC-bias, DC-offset and DC-free DoG filters in the spatial domain. **D:** Same as C, but in the frequency domain.

Figure 1C and 1D show examples of how these three concepts can be applied to DoG filters in the spatial and frequency domains, respectively. Here, with one spatial dimension, the DC-component is calculated as the signal average over the entire window. What is important to notice is that when the DoG filter is DC-free, it is a true bandpass filter since it is monotonically increasing from zero to a peak and then monotonically decreasing back to zero as illustrated in figure 1D in black.

In the present case, signals with two spatial dimensions are investigated. To take this extra spatial dimension into account, double integration of the DoG in both spatial dimensions is performed to determine if the filter is DC-free, which is the case when the result is zero:

$$\iint_{-\infty}^{\infty} e^{\frac{-(x-x0)^2+(y-yo)^2}{2\sigma_1^2}} - \delta e^{\frac{-(x-x0)^2+(y-yo)^2}{2\sigma_2^2}} = 0$$

By this reasoning, it is possible to calculate which combination of σ_1, σ_2 and δ that results in a DC-free filter as long as two of the variables are known. For example, for any given combination of σ_1 and σ_2, a δ can be calculated that achieves a DC-free filter. Figure 2A and 2B illustrates this for a size ($\sigma_{2/}$ σ_1) ratio of $\sqrt{2}$. Here, it can be seen that there is no DC-component when δ = 0.5. Figure 2B also illustrates the three bandpass parameters. Figure 2C shows the results of similar calculations in the spatial domain with a σ_1 of 1.1 with size ratio and gain ratio as shown in the Figure legend. Figure 2D is the corresponding representation in the frequency domain. Figure 2E and 2F are similar to 2C and 2D, but with a σ_1 value of 2.5. Notice that the size ratios are the same in 2C-D and 2E-F, but the response profile differs significantly. This is because the specific σ values to achieve these size ratios are not the same. This illustrates that a particular arrangement of the size and gain ratio is crucial in achieving DC-free filtering, but independent of the particular frequency sensitivity of the filters, which is closer tied to the overall size of the filter, and will be explored later.

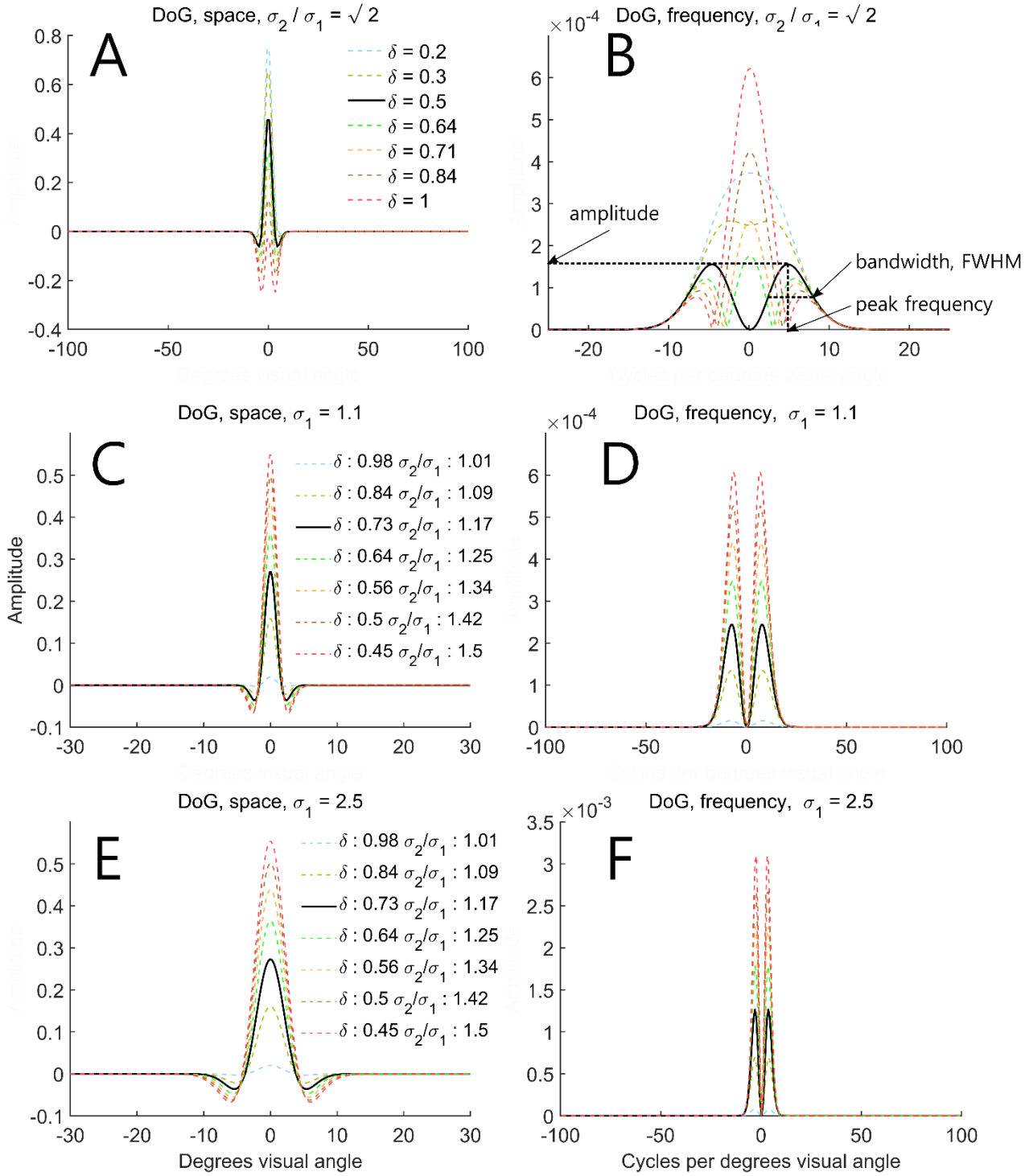

Figure 2. Size (σ_2/σ_1) and gain ratios (δ) for simulated DoG models. **A** (spatial domain) & **B** (frequency domain) show that a DoG with a size ratio $\sqrt{2}$ is DC-free when the gain ratio is 0.5, which is not the case for any of the other δ values as evidenced by the large peak around 0 in the frequency domain. **C** & **D** show that for any given size ratio, there is a corresponding gain ratio that is DC-free for filters with a σ_1 of.6. **E & F** have the same size and gain ratio as C & D, but with a σ_1 of 2.5. For all panels, legends in the spatial domain (left) also apply in the frequency domain (right).

Surround modulation modelled with DoGs has recently been extended to populations of neurons in humans using population Receptive Field (pRF) mapping with functional Magnetic Resonance Imaging (fMRI)[13]. So

in order to test these principles in human observers, we mapped the pRFs using functional magnetic resonance imaging (fMRI) in a sample of 22 healthy human subjects. Participants were placed in the bore of a Siemens Magnotom 3T Skyra. Through a mirror, they were presented with expanding/contracting rings simultaneously with clockwise/counter-clockwise rotating wedges with high-contrast ripple-like textures[14]. We also acquired high-resolution T1 structural images for each participant and used these for an anatomical reconstruction in Freesurfer. A delineation of each participant's primary visual cortex (V1) was made from a prediction using landmarks from this anatomical reconstruction using a built-in Freesurfer algorithm[15]. From these images, we were able to obtain the σ and δ parameters for voxels within each participant's V1.

For each participant, a pRF profile was created for each of 17 eccentricity bins of 1 degree visual angle (dva) for each hemisphere (0.5 – 17.5 dva). For each of these pRF profiles, we first estimated the σ_1, σ_2 and δ, and then used σ_1 and δ to compute the σ_2 that would yield a DC-free filter. Figure 3A shows the logarithmically transformed observed σ_2 plotted against the computed σ_2 (see Methods section and Supplementary Fig. 1 for examples of this calculation for individual participants without bins). From these two datasets, we then calculated their bandpass parameters (peak frequency, amplitude and bandwidth). Figure 3B-D shows the observed and the computed bandpass parameters after logarithmic transformation.

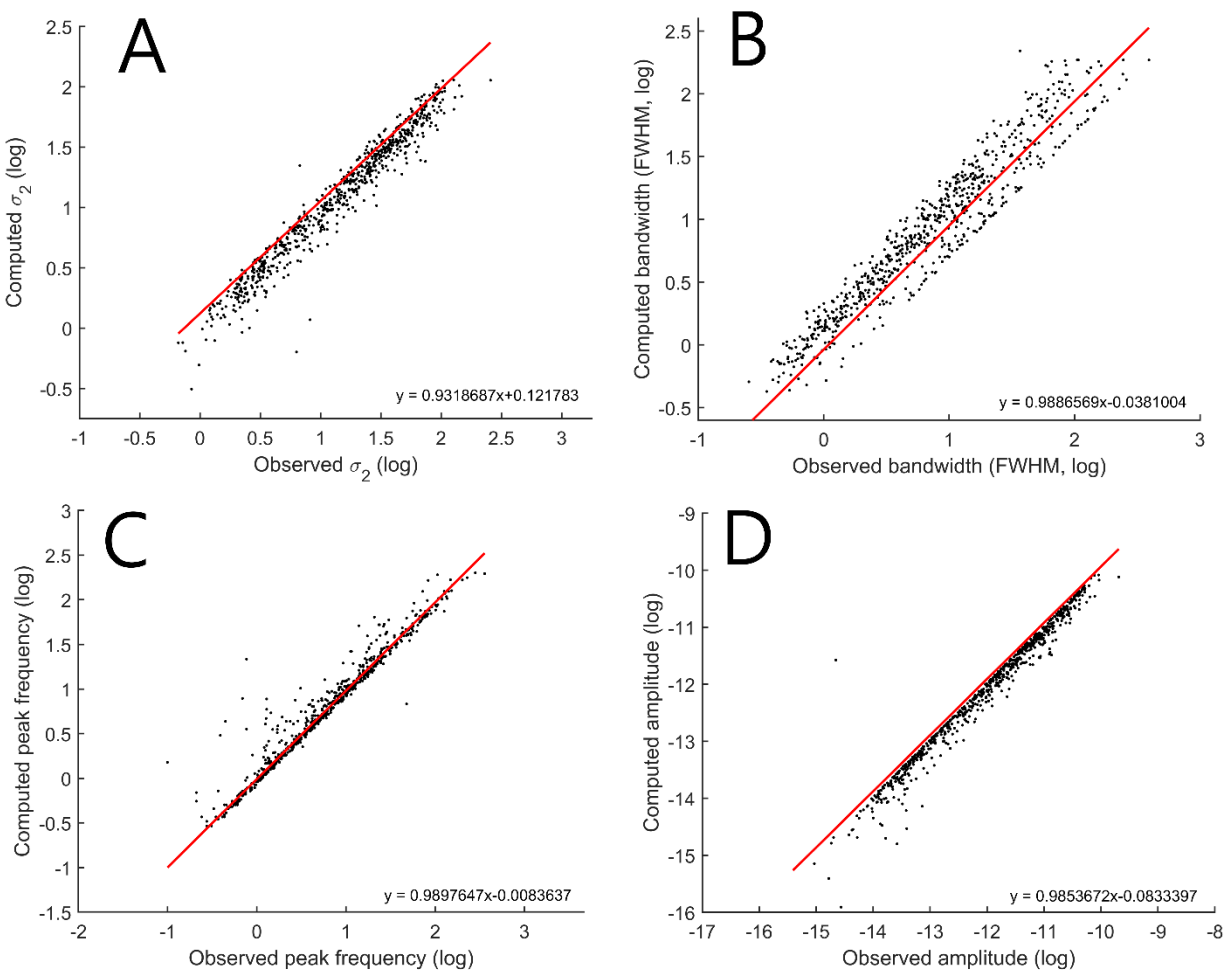

Figure 3. Observed and computed pRF parameters. A: computed σ_2 plotted against the observed σ_2. **B**, **C**, & **D:** computed compared with the observed bandpass parameters. Correlation line is plotted in red.

Random coefficient models were used to compare the observed with the computed value for a DC-free filter for each parameter separately, providing the linear fits shown in Figure 2. The results were highly significant for all parameters: σ_2 (Wald $\chi^2(1) = 1347.26$, $p < 0.00001$, slope 95% CI: 0.8821 to 0.9816, intercept 95% CI: 0.0652 to 0.1783), bandwidth (Wald $\chi^2(1) = 1403.12$, $p < 0.00001$, slope 95% CI: 0.9369 to 1.0403, intercept 95% CI: -0. 0854 to 0.0092), peak frequency (Wald $\chi^2(1) = 5621.18$, $p < 0.00001$, slope 95% CI: 0.9639 to 1.0156, intercept 95% CI: -0.0327 to 0.0160), and amplitude (Wald $\chi^2(1) = 9048.87$, $p < 0.00001$, slope 95% CI: 0.9651 to 1.0057, intercept 95% CI: -0.3308 to 0.1642). Note that for all parameters, the linear model has a near-one slope and a near-zero intercept. These findings suggest that the principle of DC-free filtering captures an important aspect of biological visual information processing.

To develop a deeper understanding of why DC-free filters are important for processing certain visual information, it is useful to examine the relationship between spatial and frequency domains through Heisenberg's uncertainty principle[16,17]. This principle asserts a fundamental limit to the certainty with which a pair of complementary variables can be known – in our case the certainty in spatial position and spatial frequency of a visual stimulus. The uncertainty principle is typically defined with Gaussian distributions, and it is custom to express the degree of uncertainty in terms of Gaussian standard deviations. Here, we examined the uncertainty principle in relation to the DoG and express the degree of uncertainty as the full width at half maximum for convenience.

Figure 4A shows the log-transformed FWHM in the frequency and the spatial domain for the observed σ_1 and σ_2 (blue circles, light blue dots) as well as the observed (black dots) and computed DoG (red dots). The anti-symmetry between the two domains that the uncertainty principle commands is confirmed by the negative relationship between all parameters; as certainty is increased in one domain, it is lowered correspondingly in the other domain.

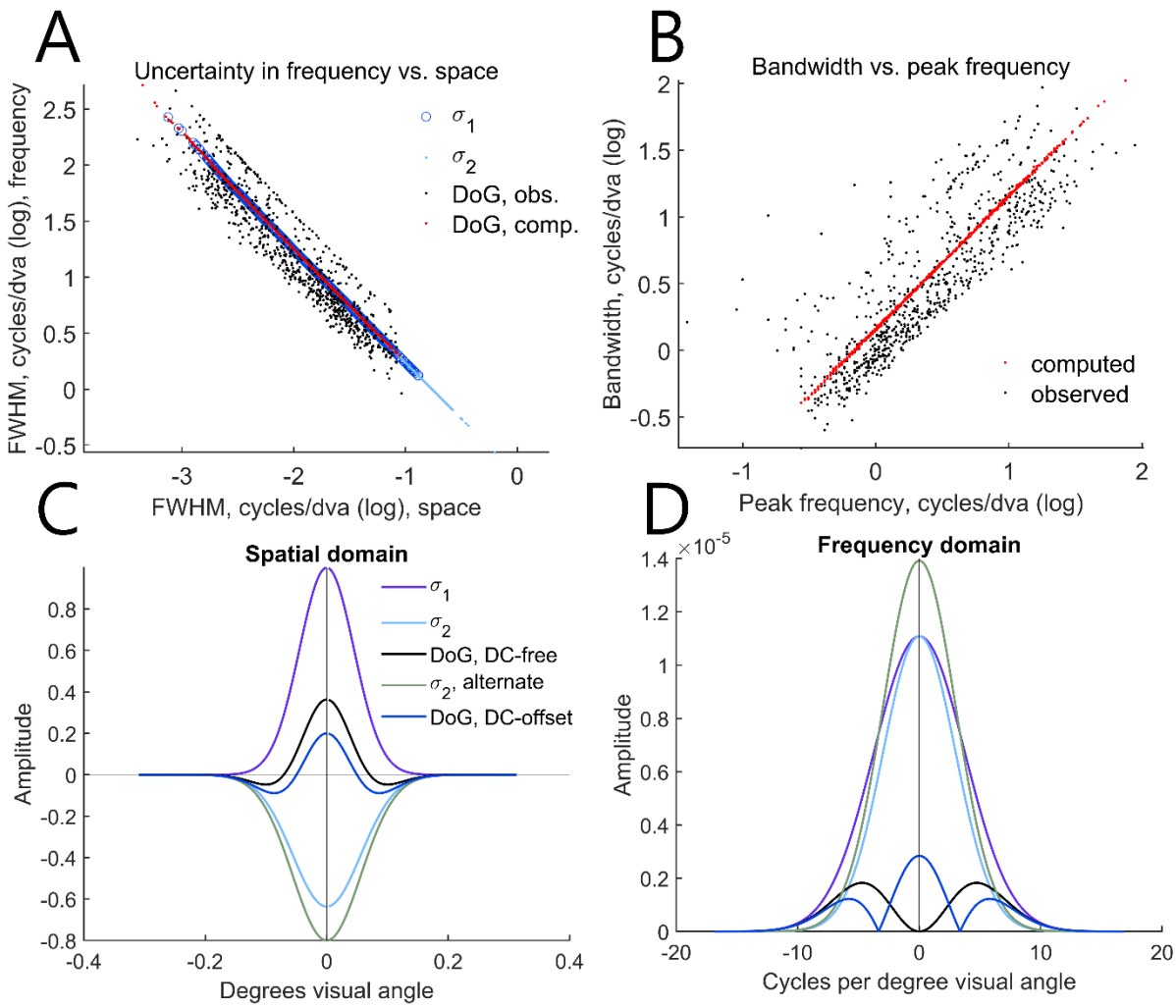

Figure 4. Uncertainty in space and spatial frequency. A: Bandwidth in FWHM of the two Gaussians, σ1 and σ2, composing the DoG as well as the bandwidth in FWHM of the observed and computed DoG filters plotted in the spatial and the frequency domain. **B**: Bandwidth compared with peak frequency for the observed and computed DoG filters. **C**: Cross-sections of the individual parts of the 2D DoG and the combined DoG for both a DC-free and a DC-offset filter plotted in the spatial domain. **D**: Same as C, but plotted in the frequency domain.

Figure 4C-D illustrates examples of this inverse relationship. These plots are cross-sections of the filter profile of single points in Figure 4A - except the alternate σ_2 (in green) which has been left out of Figure 4A for simplicity. We have included the alternate σ_2 in Figure 4C and D to illustrate how this parameter in combination with σ_1 gives a DC-offset filter as shown in black. Initially, one could be led to believe that the DC-offset DoG disobeys the uncertainty principle by being able to occupy points lower than the main diagonal of Figure 4A, but this is only because the large DC-component in the frequency domain is not taken into account when calculating the FWHM (the peak of the blue curve centred at 0 in Figure 4D).

A system processing visual information using only single Gaussians (not DoGs) could, in theory, capture high spatial frequencies to some degree. However, due to the anti-symmetry of the uncertainty principle, such an approach quickly leads to ever-smaller filters in the spatial domain which, in turn, increases the uncertainty in the frequency domain. The DC-free DoG filter circumvents this paradox by processing the same information twice. Taking the difference of two Gaussians, slightly different in size, allows the DoG filter to redistribute much of the low-frequency bandwidth towards the higher frequencies. This gives a

greater degree of certainty for the higher frequencies, and will be most efficient if the DoG filter is DC-free because a large DC-component would unnecessarily allocate a large portion of the available bandwidth to the lowest frequencies. Figure 4B illustrates how the frequency spectrum is covered by the DoG filters for our participants, but also that the higher frequencies still come with greater uncertainty (bandwidth at FWHM) than the lower frequencies.

Note that the limitations imposed by the uncertainty principle are never surpassed by DoG filtering. By allowing a slight temporal delay due to the extra computations required to process the same information twice, the limitations of the uncertainty principle can be relaxed (not shown here). This also hints at a, to our knowledge, yet to be defined extension of the uncertainty principle where the temporal domain enters alongside the trade-off between certainty in the spatial and the spatial frequency domains. In this way, the bandwidth can be distributed amongst the various domains according to the demands of a particular visual task.

Several advantages of DC-free filters have been proposed. The DC-free DoG filter is particularly suited for picking out object boundaries because these are characterised by higher spatial frequencies (the sharper the boundary, the higher the frequency) and the DoG filter is able to isolate these higher frequencies for separate processing with its bandpass characteristics. Furthermore, a DC-free DoG filter in the spatial domain ensures that the summed energy between the two individual Gaussians is zero. In the frequency domain, the amplitudes of the two Gaussians are equalised for the DC-free DoG (see Figure 4D). Together, these properties reveal a form of local contrast normalisation, which has been shown to increase performance of object feature extraction[18]. Finally, a DC-free DoG filter removes the signal constants in the spatial domain or the 0 cycles per unit distance components in the frequency domain, which can be considered a way of increasing the efficiency of the neural coding because the information contained in these signals is thought to be redundant for the proposed functions of surround modulation[19,20] – by avoiding processing of these altogether, more bandwidth can be allocated to the frequencies of interest.

Taken together, we speculate that Surround Modulation acts as a mediator between the complementary variables of the uncertainty principle according to stimulus conditions and goal of the specific visual process. This mediation can be said to be optimal when the relative strength and spatial extent of the centre and surround results in a DC-free bandpass filter that selects the spatial frequencies of interest with sufficiently high certainty in spatial position for the task at hand.

At least three prominent noise sources in this data set may explain the discrepancies between the observed and the computed data in Figure 3. The first is the pRF model-fitting procedure itself; the adopted Nelder-Nead algorithm attempts to find the global minimum in a 6-dimensional parameter-space where the initial starting point is selected by taking the best correlation between the observed signal and a rather coarse parameter space. This approach can cause the Nelder-Mead search to get caught in a local minimum and therefore fail to find the best fitting parameter set. Second, as discussed by Zuiderbaan et al.[13], neuronal position scatter might cause an increase in pRF size despite unchanged neuronal RF sizes. Finally, and perhaps most importantly, small differences between the observed and the computed values for the σ and δ parameters have a rather large impact on the bandpass parameters; because of the way we compute the bandpass parameters, this introduces a considerable amount of noise (see Methods for details).

In conclusion, we believe to have demonstrated the requirements for a typical DoG model to be DC-free and have shown that the pRF profiles of human primary visual cortex gravitate towards these requirements. We argue that the DC-free DoG filter is superior to the DC-offset DoG in its theorised functions. We further

hope to have made clear the benefits of including the uncertainty principle in the goal of understanding the functional organisation of the receptive fields of the visual system and how this organisation affects the capabilities of the visual system to process visual information. Finally, we speculate that Surround Modulation may be the mechanism which mediates these aspects of visual information processing.

References

1. Rodieck, R. W. Quantitative analysis of cat retinal ganglion cell response to visual stimuli. *Vision Res.* **5,** 583–601 (1965).

2. Hartline, H. K., Wagner, H. G. & Ratliff, F. Inhibition in the eye of Limulus. *J. Gen. Physiol.* **39,** 651–73 (1956).

3. Nelson, J. I. & Frost, B. J. Orientation-selective inhibition from beyond the classic visual receptive field. *Brain Res.* (1978). doi:10.1016/0006-8993(78)90937-X

4. Maffei, L. & Fiorentini, A. The unresponsive regions of visual cortical receptive fields. *Vision Res.* **16,** (1976).

5. Angelucci, A. & Shushruth, S. Beyond the classical receptive field: surround modulation in primary visual cortex. *new Vis. Neurosci.* 425–444 (2013). doi:10.1016/S0079-6123(01)34012-8

6. Hines, M. Line spread function variation near the fovea. *Vision Res.* **16,** (1976).

7. Wilson, H. R. QUANTITATIVE CHARACTERIZATION OF TWO TYPES OF LINE-SPREAD FUNCTION NEAR THE FOVEA. (1978).

8. Dacey, D. *et al.* Center surround receptive field structure of cone bipolar cells in primate retina. *Vision Res.* **40,** 1801–1811 (2000).

9. Cavanaugh, J. R., Bair, W. & Movshon, J. A. Nature and Interaction of Signals From the Receptive Field Center and Surround in Macaque V1 Neurons. *J. Neurophysiol.* **88,** 2530–2546 (2002).

10. Angelucci, A. *et al.* Circuits and Mechanisms for Surround Modulation in Visual Cortex. *Annu. Rev. Neurosci.* **40,** 425–451 (2017).

11. Enroth-Cugell, C. & Robson, J. G. The contrast sensitivity of retinal ganglion cells of the cat. *J. Physiol.* **187,** 517–552 (1966).

12. Schouhamer Immink, K. A. & Pátrovics, L. Performance assessment of DC-free multimode codes. *IEEE Trans. Commun.* **45,** 293–299 (1997).

13. Zuiderbaan, W., Harvey, B. M. & Dumoulin, S. O. Modeling center – surround configurations in population receptive fields using fMRI. *J. Vis.* **12,** 1–15 (2012).

14. Schwarzkopf, D. S., Anderson, E. J., de Haas, B., White, S. J. & Rees, G. Larger Extrastriate Population Receptive Fields in Autism Spectrum Disorders. *J. Neurosci.* **34,** 2713–2724 (2014).

15. Hinds, O. P. *et al.* Accurate prediction of V1 location from cortical folds in a surface coordinate system. *Neuroimage* (2008). doi:10.1016/j.neuroimage.2007.10.033

16. Heisenberg, W. The actual content of quantum theoretical kinematics and mechanics. *Zeitschrift für Phys.* (1927). doi:10.1119/1.1991172

17. Kennard, E. H. Zur Quantenmechanik einfacher Bewegungstypen. *Zeitschrift für Phys.* (1927). doi:10.1007/BF01391200

18. Dalal, N. & Triggs, B. Histograms of oriented gradients for human detection. in *Proceedings - 2005 IEEE Computer Society Conference on Computer Vision and Pattern Recognition, CVPR 2005* (2005). doi:10.1109/CVPR.2005.177

19. Barlow, H. B. Possible Principles Underlying the Transformations of Sensory Messages. *Sens. Commun.* 216–234 (1961). doi:10.7551/mitpress/9780262518420.003.0013

20. Field, D. J. Relations between the statistics of natural images and the response properties of cortical cells. *J. Opt. Soc. Am. A* **4,** 2379 (1987).

Methods

Participants

This study was approved by the local ethics committee, De Videnskabsetiske Komitéer for Region Midtjylland, and conducted according to the principles of the Declaration of Helsinki. 24 healthy, right-handed adults with normal or corrected-to-normal visual acuity aged between 18 and 40 (14 females) gave informed consent to participate in the study. 2 participants were excluded because we failed to generate a meaningful pRF map for either one or both hemispheres.

MRI and stimuli

The stimuli were similar to those used in conventional retinotopic mapping[1] and consisted of expanding/contracting rings and clockwise/counterclockwise rotating wedges with a high-contrast ripple-like texture and mean luminance of 87 cd/m^2. The stimuli subtended a maximum of 17.4° visual angle.

Procedure

Participants were placed in the bore of a Siemens Magnetom Skyra 3T MRI scanner. Stimuli were projected onto a screen in the back of the scanner and viewed by the participant through a mirror placed on top of the head coil. Participants were instructed to maintain fixation on a small black dot in the centre of the screen and at pseudo-random intervals, the dot would change colour to red. To control eye-fixation and overt attention, participants were instructed to press a button when this occurred.

Stimulus presentation and recording of behavioural responses was implemented using the Psychophysics Toolbox 3 [2,3] running under MATLAB 2013a. Population Receptive Field mapping was implemented using custom scripts. fMRI images were acquired using a 32-channel head coil with the top removed (for better participant view) resulting in 20 remaining channels.

176 whole-brain volumes of high-resolution structural images were acquired using a T1-weighted coronal-oriented MP2RAGE sequence (TR: 5000ms, TE: 2.98ms; field of view: 240 x 256 x 176mm, voxel size: 1mm^3 isotropic) using a 32-channel head coil.

The pRF mapping protocol acquired 15 continuous axial slices (slice-thickness: 2mm) for each volume using a T2*-sensitive gradient echoplanar Imaging (EPI) sequence (TR: 1000 ms; TE: 30 ms; flip angle: 60°; field of view: 192 x 192 x 30 mm; voxel size: 2x2x2 mm, GRAPPA with PAT-factor 2). 6 runs of 225 volumes were acquired for each participant (3 clockwise and 3 counter-clockwise).

MRI analysis

Image preprocessing was carried out using Statistical Parametric Mapping (SPM12; Wellcome Department of Imaging Neuroscience, London, UK) running under MATLAB R2013a. For each participant, volumes from the pRF mapping were realigned to the first image of the run to correct for head motion, unwarped using a presubstracted phase and magnitude B_0 field map to correct for geometric distortions, and slice-time corrected for acquisition delays. Next, the first image of the first run was coregistered to the high-resolution structural and subsequently these coregistration parameters were applied to all other images from the remaining runs. The structural images were used for cortical reconstruction and volumetric segmentation within the Freesurfer image analysis suite[4,5] to create an inflated 3D image of the grey/white-matter boundary for each participant. Based on this reconstruction, a prediction of the anatomical extent of V1 was created using a built-in Freesurfer algorithm[6]. This V1 delineation was used as a mask for constraining which voxels to include in the following pRF analysis.

pRF analysis

A full account of the pRF analysis procedure has been given by Dumoulin and Wandell[7,8]. In brief, we modelled the measured fMRI signal as

$$y(t) = p(t)\beta + e$$

where $p(t)$ is the predicted BOLD signal in each voxel at time t, β is a scaling coefficient that accounts for unknown units of the BOLD signal and e is the residual error. The predicted response $p(t)$ was calculated by modelling the receptive field of the neuronal population within each voxel using a two-dimensional Difference of Gaussians of the form

$$f(x,y) = e^{\frac{-(x-x0)^2+(y-yo)^2}{2\sigma_1^2}} - \delta e^{\frac{-(x-x0)^2+(y-yo)^2}{2\sigma_2^2}}$$

where σ_1 and σ_2 is the standard deviations of the two Gaussians and δ is a parameter that modulates the amplitude of the second negative Gaussian. This model was combined with a matrix representation of the stimulus intensity at (x,y) for all time points in the acquired volumes. The result was summed for each volume and then convolved with SPMs standard hemodynamic model, and finally scaled with β. We used Matlab's implementation of the Nelder-Mead method (fminsearch) to obtain the pRF model parameters that best fit the data by minimizing the sum of squared error between the observed and predicted response.

DC-balance

The results of the pRF analysis yielded a σ_1, σ_2, δ, x- and y coordinate for each of the included voxels. To compute the values of $\sigma1$, $\sigma2$, and δ that would result in a DC-balanced filter, we used the observed σ_1 and δ values in a Nelder-Mead search algorithm that minimized the squared integral of the pRF parameters of individual voxels and allowed σ_2 to vary. Supplementary figure 1 shows the result of this calculation for both hemispheres from two participants. There is a clear tendency towards agreement between the observed and the computed data, albeit with some additional noise.

For both the observed and the computed pRF parameters, we calculated their bandpass parameters by first transforming the data into a 2D discrete Fourier space and since the DoG is circularly symmetric in Fourier space, we used Matlabs findpeaks function to find the signal maximum (amplitude) on the centremost 1D representation of the absolute signal. From this peak we observed the corresponding peak frequency and calculated the full-width at half its maximum. Note that for the DoG in the spatial domain, the half maximum is defined as the point that falls half the distance between the DoG minimum and maximum. This is because this is the only case where the filter falls below zero (see figure 3C).

Small differences between the observed and computed σ and δ parameters have a rather large impact on the bandpass parameters – especially the bandwidth. The main reason for this is shown in supplementary figure 2, and is connected to the way we compute the bandpass parameters; when a DC-bias is introduced in the bandpass filter, this may easily lead to a situation where the filter does not fall below the half-maximum point in the FWHM calculation and therefore the bandwidth is overestimated as exemplified in supplementary figure 2B. An underestimation of the bandwidth is also seen when a strong DC-component is observed at the lowest frequencies as in supplementary figure 2A and C.

To increase the signal to noise ratio, we pooled the data into eccentricity bins. Since pRF size is known to be relatively stable across polar angle for a given eccentricity in pRF experiments[7], we created 17 eccentricity bins of 1 degree visual angle each (from 0.5 to 17.5) and removed voxels with model fits that did not, at least, explain 5% of the BOLD signal variance. By inspecting plots of the individual DoG model parameter distribution, it was observed that they were not all normally distributed, so in these cases we used the median value within bins. In 741 out of 748 (22 participants x 2 hemispheres x 17 eccentricity bins), this procedure lead to non-zero parameter estimates, and these data points were used in further analysis.

Statistical analysis

Observed parameter values were log-transformed and normality was inspected using histograms and qq-plots. Data appeared normally distributed, apart from a small fraction of data points showing very large deviations (22 of 741, less than 3%, typically for the peak frequency parameter) indicative of poor pRF model fits. These were rejected before statistical modelling. Data were analysed in a random coefficient model with (log-transformed) observed parameter value as the dependent variable, (log-transformed) simulated parameter value as a covariate and random intercepts and slopes varying with Participant and Hemisphere within Participant. Whenever possible, residual error correlations were allowed to decrease exponentially with increasing difference in Eccentricity (for peak frequency, this model did not converge, and to ensure convergence, no assumptions was made for residual error correlations). Model fits were made using restricted maximum likelihood function with the Broyden-Fletcher-Goldfarb-Shanno (BFGS) algorithm.

Code availability

The custom code used to support the findings of this study is available from the corresponding author upon reasonable request.

1. Sereno, M.I., Dale, A.M., Reppas, J.B., Kwong, K.K., Belliveau, J.W., Brady, T.J., Rosen, B.R.and Tootell, R. B. H. Borders of Multiple Visual Areas In Humans Revealed By Functional MRI. *Science (80-.).* **268,** 889–893 (1995).

2. Brainard, D. H. The Psychophysics Toolbox. *Spat. Vis.* **10,** 433–436 (1997).

3. Pelli, D. G. The VideoToolbox software for visual psychophysics: transforming numbers into movies. *Spat. Vis.* **10,** 437–442 (1997).

4. Dale, A. M., Fischl, B. & Sereno, M. I. Cortical surface-based analysis. I. Segmentation and surface reconstruction. *Neuroimage* **9,** 179–194 (1999).

5. Fischl, B., Sereno, M. I. & Dale, A. M. Cortical surface-based analysis. II: Inflation, flattening, and a surface-based coordinate system. *Neuroimage* **9,** 195–207 (1999).

6. Hinds, O. P. *et al.* Accurate prediction of V1 location from cortical folds in a surface coordinate system. *Neuroimage* (2008). doi:10.1016/j.neuroimage.2007.10.033

7. Dumoulin, S. O. & Wandell, B. a. Population receptive field estimates in human visual cortex. *Neuroimage* **39,** 647–60 (2008).

8. Harvey, B. M. & Dumoulin, S. O. Modeling center – surround configurations in population receptive fields using fMRI Wietske Zuiderbaan. *J. Vis.* **12,** 1–15 (2012).